Comparative analysis of morphology 1D and 2D particles effect in starting powders on microstructure and thermoelectric properties of grained Bi2Te2.7Se0.3 compound

Maxim Yaprintsev [a], Alexei Vasil'ev [b], Oleg Ivanov [a,b,*], Daniil Popkov [a], Egor Kudryavtsev [a]

[a] *Belgorod State University, Belgorod, 394015, Russian Federation*
[b] *Belgorod State Technological University named after V.G. Shukhov, Belgorod, 308012, Russian Federation*

ARTICLE INFO

ABSTRACT

Features in microstructure and thermoelectric properties of grained $Bi_2Te_{2.7}Se_{0.3}$ compound, prepared by spark plasma sintering of starting powders with various morphologies, are comparatively examined. The 1D samples, prepared from the starting powder consisting of 1D bar-shaped particles, were weakly-textured (orientation factor is equal to ~0.07) and preferentially consisted of bar-shaped grains. The 2D samples, prepared from the starting powder consisting of 2D plate-shaped particles, were highly-textured (orientation factor is equal to ~0.28) and consisted of plate-shaped grains. Both weakly-textured 1D sample and highly-textured 2D sample demonstrated remarkable anisotropy in the behavior of their transport properties (specific electrical resistivity and total thermal conductivity). For highly-textured sample, this anisotropy is a typical phenomenon, resulting from recovering in crystal anisotropy, which is inherent for single-crystalline Bi_2Te_3-based material. For the weakly-textured 1D sample, the anisotropy in the transport properties is unexpected enough. In this case, anisotropy can be attributed to the anisotropic grain size effect on the transport properties. This effect is due to a different number of grain boundaries, overcome by the electrons or phonons under different measuring orientations. The highest value of the thermoelectric figure-of-merit (~0.68) was found for the 1D and 2D samples and at perpendicular measuring orientation.

1. Introduction

Features in the grain structure of a grained material are characterized by the shape and size of grains, a degree of grain ordering, properties of grain boundaries, etc. Many physical properties of structural and functional materials are crucially dependent on these features [1–10]. By tuning grain structure in the desired manner, these properties can be effectively varied and optimized. In particular, grain engineering approaches are prospective and fruitful ways to affect the thermoelectric properties (the specific electrical resistivity, ρ, the Seebeck coefficient, S, and the total thermal conductivity, k_t) of grained material [11–18]. The ρ, S, and k_t properties should be optimally combined in thermoelectric material to maximize its thermoelectric figure-of-merit, $ZT = (S^2 \cdot T)/(\rho \cdot k_t)$, where T is the absolute temperature. First of all, grain boundaries or boundaries between different phases in multi-phased compounds can act as effective scattering centers for electrons and phonons, affecting ρ and k_t [19–22]. Besides, energy filtering of

electrons, which is overcome by tunneling a potential barrier corresponding to the grain boundary, can affect S [23–25]. Finally, grain ordering in some thermoelectric materials, which are readily texturing under uniaxial mechanical loading during the preparation of these materials, can result in the development of anisotropy in the thermoelectric properties [26–30]. This anisotropy is an additional tool to enhance ZT, too.

Grain structure with desired properties can be often governed by parameters and properties of particles in a starting powder, applied to sinter relevant grained material. That is the morphology of grains (size and shape) in grained material will be dominantly originated from the morphology of particles (size and shape) in starting powder. To activate this "particles" → "grains" link, specific technological ways, preventing sufficient changes of the original shape and size of the particles during high-temperature recrystallization, should be applied. Spark plasma sintering (SPS) of starting powders during the preparation of relevant grained material is positively characterized by a very short time of

---

sintering process that allows effective depressing of this recrystallization [31,32].

In the present work, the SPS method was applied to examine the morphology of 1D or 2D particles effect in starting powders on the microstructure and thermoelectric properties of grained $Bi_2Te_{2.7}Se_{0.3}$ compounds. Today, this compound is the best material with electronic conductivity for various low-temperature applications [33,34]. Its thermoelectric properties are known to be dependent on the parameters of grain structure [35–37]. One can expect that grain structures of compounds, prepared from starting powders with different morphology of particles, will be different, too. The difference in grain structures will result in a relevant difference in the thermoelectric properties. The main aim of this paper is to comparatively analyze features in the grain structures and thermoelectric properties of grained $Bi_2Te_{2.7}Se_{0.3}$ compounds, which are governed by a chain of "morphology of particles in starting powder" → "morphology of grains in relevant grained material" → "thermoelectric properties of grained material".

2. Materials and methods

Chemicals. All chemical reagents used in this study were of analytical grade. Bismuth nitrate pentahydrate ($Bi(NO_3)_3 \cdot 5H_2O$), tellurium dioxide (TeO_2), selenium dioxide (SeO_2), and sodium hydroxide (NaOH) were purchased from Chemcraft LLC. Ethanol and 1,2-ethanediol were purchased from JSC EKOS-1. Two different technological routes were involved to prepare starting $Bi_2Te_{2.7}Se_{0.3}$ powders with different morphology of the particles. To prepare starting powder consisting of the 1D bar-shaped particles (the starting 1D powder), a two-stage process was applied. The Te+10 at. % Se particles were synthesized at the first stage. Analytically pure TeO_2 and SeO_2 oxides, taken for the desired Te+10 at. % Se ratio was first dissolved in the 300 cm^3 ethane-1,2-diol and 15 g NaOH mixture under vigorous stirring by a magnetic stirrer. After, the mixture was put in a flask, equipped with reflux, and maintained at 160°C for 2 h. As a result, the Te+10 at. % Se particles were synthesized in the reaction medium. During the second stage, these particles were next applied as a precursor to synthesize starting $Bi_2Te_{2.7}Se_{0.3}$ powder. To do so, $(Bi(NO_3)_3 \cdot 5H_2O$ was quantitatively added to the Te+10 at. % Se medium, which was finally maintained at 180°C for 4 h. After completing the synthesis reaction, a dark grey precipitate consisting of the $Bi_2Te_{2.7}Se_{0.3}$ particles was taken out by centrifuging and washed with deionized water and ethyl alcohol several times and then dried at 60°C for 8 h. In contrast to the two-stage synthesis of starting 1D powder, starting powder consisting of the 2D plate-shaped particles (starting 2D powder) was synthesized by using one process. First, $Bi(NO_3)_3 \cdot 5H_2O$, TeO_2, and SeO_2, taken in desired stoichiometric ratio, were dissolved in the 600 cm^3 ethane-1,2-diol NaOH and 15 g NaOH mixture under vigorous stirring by a magnetic stir. Then, the mixture was put in a flask, equipped with reflux, and maintained at 180°C for 6 h. As result, the $Bi_2Te_{2.7}Se_{0.3}$ particles were synthesized. After the synthesis of these particles, further treatment of starting 2D powder, including centrifuging, washing, and drying stages was carried out in the manner described above for starting 1D powder. The technological routs, applied to prepare starting 1D and 2D powders, are schematically presented in Fig. 1. To not complicate Fig. 1, the routs are presented for the synthesis of starting Bi_2Te_3 powders with different morphology of the particles. To transfer to the synthesis of starting $Bi_2Te_{2.7}Se_{0.3}$ powders in Fig. 1, Se should be just added to Te. Starting powders with different morphology of the particles were spark-plasma-sintered. The process of spark plasma sintering (SPS) was carried out using a SPS Model 10-3 (Thermal Technology, LLC). The SPS process was implemented at a pressure of 40 MPa and a temperature of 680 K for 2 min in a vacuum, resulting in the Ø20 mm × 15 mm cylinders.

Archimedes' method was applied to measure the density of samples using a device ASP 3.1 (LLC Porotech). To identify the crystal structure, and phase composition of starting powders with different morphology of the particles and relevant bulk samples, X-ray diffraction (XRD) analysis was performed by using a diffractometer Ultima IV (Rigaku) with CuK_α-radiation (wave length, λ, for CuK_α radiation is 0.15418 nm, angular range is from 5 to 80 2θ, angular step is 0.01 θ, power is 1.6 kW (40 kV, 40 μA)). The Rietveld method using the PDXL (Rigaku) software was applied to refine the experimental XRD patterns. To analyze the morphology of the particles in starting powders, estimate average particle size, and examine grain structure features in bulk samples, scanning electron microscopy (SEM) was applied by using a microscope Nova NanoSEM 450 (FEI) (high voltage is 30 kV and working distance is 10 mm). Transmission electron microscopy (TEM) using a microscope JEM – 2100 (JEOL) was applied to characterize a growth direction in the particles with different dimensionality (high voltage is 200 kV, diffraction length for selected area electron diffraction is 100 cm). The energy dispersive X-ray spectroscopy (EDX) method by using an INCAEnergy spectrometer for transmission electron microscopy (Oxford Instruments) was applied to map distributions of chemical elements for the particles in starting 1D and 2D powders. The Bi-L, Sm-L, Te-L, and Se–K characteristic lines were used to plot the maps. To determine the correct elemental composition of bulk samples, prepared from starting 1D and 2D powders, an ICP (Inductively Coupled Plasma) emission spectrometer ICPE-9000 (Shimadzu) was applied. For each sample, 3 parallel measurements were taken using the axial survey method.

To examine the transport properties of bulk samples, prepared from starting 1D and 2D powders (1D and 2D samples), 2 × 2 × 10 mm bars
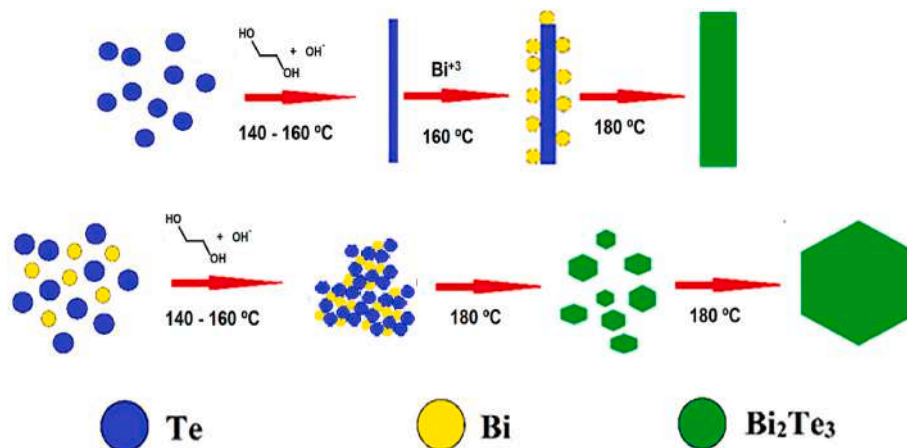

Fig. 1. Schematics of synthesis of starting Bi_2Te_3 powders, consisting of the 1D bar-shaped particles (top schematic) and the 2D plate-shaped particles (bottom schematic).

and Ø10 × 2 mm disks were prepared. A system ZEM-3 (ULVAC Advance-Riko) was applied to measure the specific electrical resistivity of bar samples by using the four-probe method, whereas a thermal constant measurement system TC-1200RH (ULVAC Advance-Riko) was applied to measure the total thermal conductivity of disk-shaped samples by using laser flash method under vacuum. The $\rho(T)$, $S(T)$, and $k_t(T)$ dependences were taken for temperatures from 290 to 560 K. Taking into account the system accuracy and the measurement precision, an error of ca. 5% in the Seebeck coefficient measurement and an error of ca. 1% in the electrical resistivity measurement were estimated. The thermal diffusivities was measured with an estimated error of ca. 5%.

3. Results and discussion

3.1. Characterization of starting 1D and 2D powders

By the XRD pattern (Fig. 2), the Te+10 at. % Se particles, applied as a precursor to prepare starting 1D $Bi_2Te_{2.7}Se_{0.3}$ powder, corresponded to single hexagonal $P3_121$ phases with unit cell parameters $a = b = 4.457$ Å and $c = 5.929$ Å. SEM image of several particles, extracted from a liquid reaction medium, is shown in the inset to Fig. 2. To not complicate the Figure, only the highest peaks in the XRD pattern were indexed. The XRD pattern was fitted by the Rietveld treatment (Fig. S1). All the peaks correspond to single hexagonal $P3_121$ phase. The particles are 1D-whiskers with lengths of several μm and thicknesses of ~100 nm.

Starting 1D and 2D powders were also single rhombohedral phases with space $R\bar{3}m$ symmetry. XRD patterns for these powders were the same. For example, the XRD pattern, taken for starting 1D powder, is
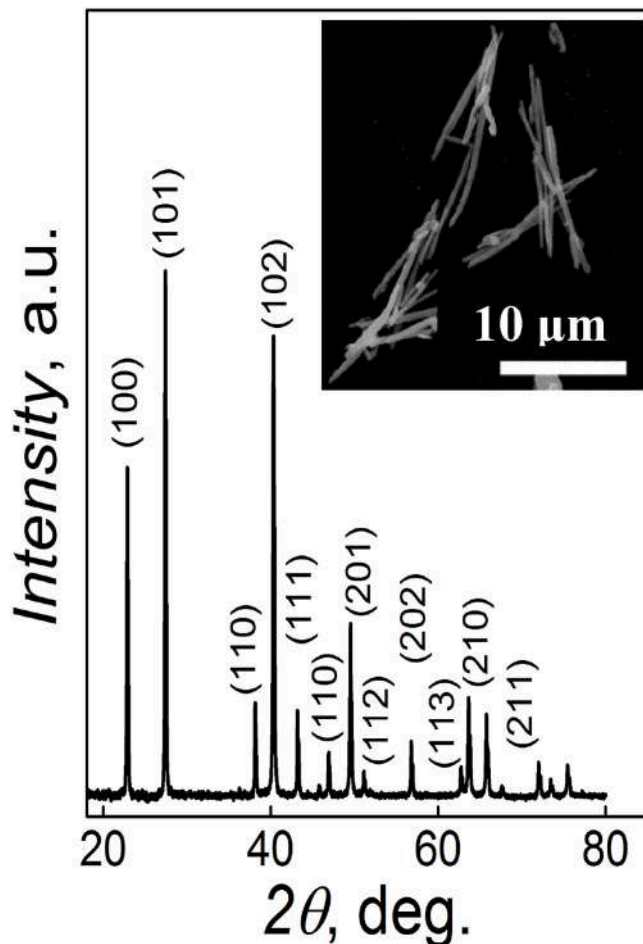
shown in Fig. 3 (a). By SEM data, starting 1D powder consists of bar-shaped particles (Fig. 3 (c)), whereas starting 2D powder consists of hexagonal plate-shaped particles (Fig. 3 (d)). According to the results of selected area electron diffraction (SAED), taken for the individual 1D and 2D particles (Fig. 4 (a) and (b)), the particles are single-crystalline with crystal Bi_2Te_3 structure. The 1D bars are elongated along [001] direction or crystal *c*-axis, and the 2D plates correspond to (110) plate or crystal (*a-b*)-plane. In other words, the crystal *c*-axis was oriented perpendicularly to the bigger surface of the 2D plates. Taking into account the specific shape of the particles in 1D and 2D powders, two sizes, L_a and T_a, for the particles in these powders were estimated. The L_a size is the average length of the bar-shaped particles or the average lateral size of the plate-shaped particles. The T_a size is the average thickness of both types of particles. To extract the L_a and T_a values, histograms of relevant size distributions were plotted by using SEM images of 1D and 2D particles.

The histograms were fitted in frames of lognormal unimodal distribution [38].

$$F(L \text{ or } T) = \frac{1}{\sqrt{2\pi}\ln\sigma(L \text{ or } T)}\exp\left(-\frac{(\ln(L \text{ or } T) - \ln(L_a \text{ or } T_a)^2}{2(\ln\sigma(L \text{ or } T)^2}\right) \quad (1)$$

where $F(L \text{ or } T)$ is the lognormal probability density function, $\ln(L_a \text{ or } T_a)$ and $\ln\sigma(L_a \text{ or } T_a)$ are logarithms of mean and standard deviation of relevant sizes for the bar-shaped or plate-shaped particles.

The L_a and T_a values for the bar-shaped and plate-shaped particles, extracted by expression (1), are collected in Table 1. Since $L_a \gg T_a$ for both types of particles, one can conclude that the bar-shaped particles and the plate-shaped particles are 1D and 2D objects, respectively. According to EDX mapping of the Bi, Te, and Se distributions, taken for individual particles in starting 1D and 2D powders, all the elements are uniformly distributed within the bar-shaped (Fig. 5) or the plate-shaped particles (Fig. 6).

3.2. Features in the microstructure of 1D and 2D samples

The bulk $Bi_2Te_{2.7}Se_{0.3}$ materials, SPS-prepared from the 1D and 2D starting powders, were dense enough. The density value for both types of samples was estimated as ~7.5 g·cm^{-3} which is ~96% of the theoretical value of the $Bi_2Te_{2.7}Se_{0.3}$ density (7.78 g/cm^3). Correct elemental composition of the 1D and 2D samples were determined by ICP emission

Fig. 2. XRD pattern was taken for the Te+10 at. % Se precursor. Inset is an SEM image of the precursor, consisting of 1D-whiskers.
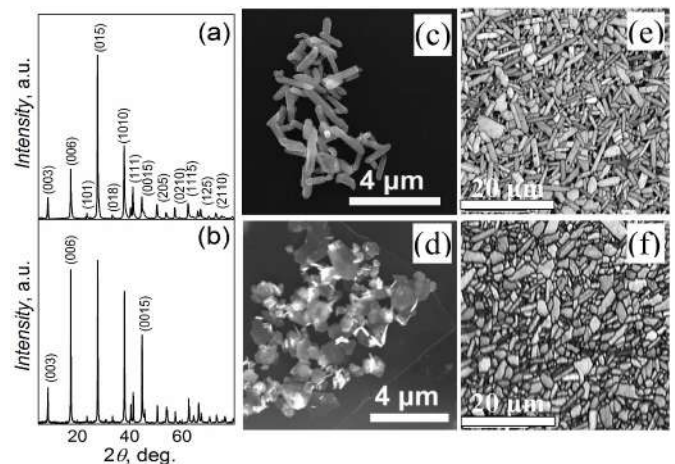
Fig. 3. XRD patterns, taken for 1D starting $Bi_2Te_{2.7}Se_{0.3}$ powder (a) and from the fractured surface of highly-textured 2D $Bi_2Te_{2.7}Se_{0.3}$ sample, which is oriented perpendicularly to SPS-pressing direction (b); SEM images of the 1D bar-shaped $Bi_2Te_{2.7}Se_{0.3}$ particles (c) and the 2D plate-shaped particles (d); SEM images, taken on fractured surfaces of weakly-textured 1D (e) and highly-textured 2D (f) $Bi_2Te_{2.7}Se_{0.3}$ samples (surfaces are oriented perpendicularly to SPS-pressing direction).
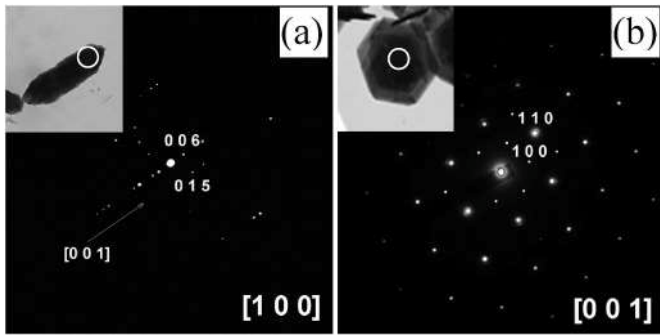
Fig. 4. SAED patterns, taken for individual 1D (a) and 2D (b) particles. TEM images of the particles are shown in relevant insets to Figures. Circles in the insets correspond to areas, applied to observe electron diffraction.

Table 1
Parameters of characterization of 1D and 2D starting powders (average sizes of the particles) and 1D and 2D bulk samples (characteristics of grain structure and anisotropy coefficients of the transport properties).

Samples	Starting powders		Bulk samples					
	L_a, μm	T_a, μm	D_l, μm	D_t, μm	D_l/D_t	LF	$\rho_{||}/\rho_\perp$	$k_{t\perp}/k_{t||}$
1D	1.18	0.290	9.10	0.93	9.8	0.07	1.76	1.45
2D	0.67	0.065	2.25	0.35	6.4	0.28	1.55	1.45
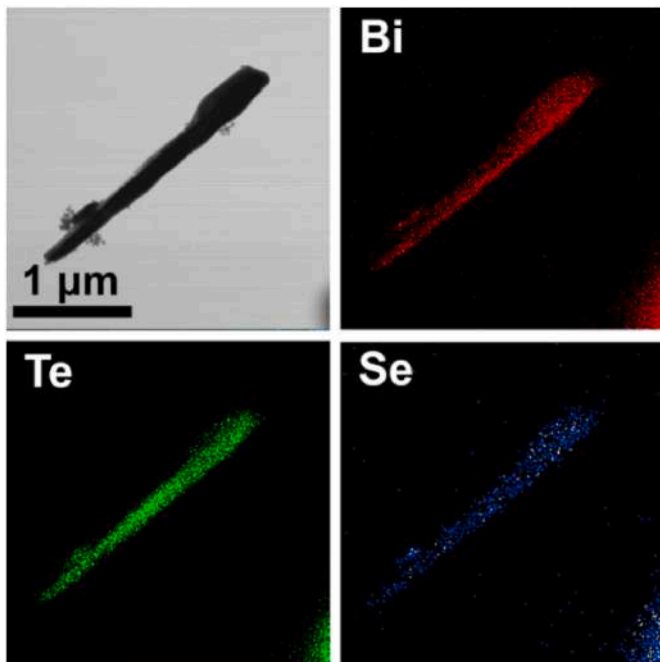
Fig. 5. Maps of the Bi, Te, and Se distributions, taken within individual bar-shaped $Bi_2Te_{2.7}Se_{0.3}$ particle, which is shown in the TEM image.

Fig. 6. Maps of the Bi, Te, and Se distributions, taken within individual plate-shaped $Bi_2Te_{2.7}Se_{0.3}$ particle, which is shown in the TEM image.

spectroscopy. The 1D sample was found to be Te-rich. Its correct chemical composition corresponds to $Bi_2Te_{2.7+\delta}Se_{0.3}$, where $\delta \approx 0.07$ (~1.4 at. %). The 2D sample is Te-deficient with correct $Bi_2Te_{2.7-\delta}Se_{0.3}$ composition, where $\delta \approx 0.04$ (~0.8 at. %). This difference in Te content can be originated from different technological routes, applied to prepare starting 1D and 2D powders. It should be noted that interstitial Te atoms and anti-site Te_{Bi} defects are specific for Te-rich composition, whereas Te-vacancies and anti-site Bi_{Te} defects are specific for Te-deficient

composition [39–42].

The sample prepared from the 1D bar-shaped particles (1D sample) preferentially consisted of elongated grains having the shape of bars. Besides the bar-shaped grains, other grains with irregular shapes are also formed under the SPS process. The sample, prepared from the 2D plate-shaped particles (2D sample), preferentially consisted of plate-shaped grains. Therefore, the morphology of the grains in bulk 1D and 2D samples is governed by the morphology of the particles in relevant starting powder. It should be noted that the bar-shaped and plate-shaped grains form lamellar sheets, oriented perpendicularly to the SPS-pressing direction. The features in the grain structure of 1D and 2D samples, listed above, are observed in SEM images, taken on fractured surfaces of these samples (Fig. 3 (e) and (f)). These images are top images of the lamellar sheets, consisting of the bar-shaped (Fig. 3 (e)) and plate-shaped (Fig. 3 (f)) grains. Similarly to the particles in starting $Bi_2Te_{2.7}Se_{0.3}$ powders, two characteristic sizes, D_l and D_t, for the grains in 1D and 2D samples were also estimated. The D_l size is the average length of the bar-shaped grains or the average lateral size of the plate-shaped grains, and the D_t size is the average thickness of both types of grains. The D_l and D_t values, extracted for 1D and 2D samples, are collected in Table 1. By comparing D_l and D_t, one can conclude that the grains in the 1D sample are 1D objects, and the grains in the 2D sample are 2D objects. A grain shape factor, introduced as D_l/D_t, is much higher for the 1D sample.

XRD pattern, taken on the fractured surface of the 2D sample, which is oriented perpendicularly to the SPS-pressing direction, is shown in Fig. 3 (b). Compared to the powder XRD pattern, intensities of (00l) peaks in this XRD pattern are remarkably enhancing. This change in the XRD pattern is due to grain ordering under texturing. Namely, crystal c-axes of the grains in the textured sample are preferentially directed parallel to the SPS-pressing direction (or perpendicularly to the lamellar sheets), while crystal (a-b)-planes of the grains are preferentially oriented perpendicular to this direction (or parallel to the sheets). In contrast to the 2D sample, the 1D sample was far less textured. The degree of grain ordering for both samples was characterized by the Lotgering factor, LF [43]. For the highly-textured 2D sample, LF was equal to ~0.28, whereas for the weakly-textured 1D sample LF was equal to ~0.07. Unit cell parameters, $a = b$, and c, for 1D and 2D

samples, calculated by the Rietveld refinement, were equal to 4.374 and 30.464 Å, and 4.377 and 30.467 Å for 1D and 2D samples, respectively. Hence, the unit cell of the 2D sample is slightly expanded as compared to that of the 1D sample.

This feature can be related to different Te content in 1D Te-rich and 2D Te-deficient samples. Anti-site defects of Bi in Te-sites (Bi_{Te}) are typical defects in the Te-deficient sample. Ionic radii, R, of Bi^{3+} and Te^{2+} in crystal Bi_2Te_3 structure are remarkably different, $R(Bi^{3+}) = 1.020$ nm against $R(Te^{2+}) = 0.089$ nm [44]. Since $R(Bi^{3+})$ is bigger as compared to $R(Te^{2+})$, forming of Bi_{Te} defects will be accompanied by increases in unit cell parameters.

To correctly examine the grain orientations in weakly-textured 1D and highly-textured 2D samples, EBSD-SEM maps were taken from thoroughly polished surfaces, which are oriented perpendicularly and parallel to the SPS-pressing direction (Fig. 7).

These maps show the distribution of crystallographic orientations for the surface grains. The color of individual grain is directly connected with its crystallographic orientation by the inset to Fig. 7. One can see that the 2D sample is highly-textured and the texturing axis is parallel to the SPS-pressing direction, i.e., it coincides with the crystal c-axis. No preferential orientation of the bars-grains is observed in the 1D sample, although the bar-shaped grains are highly anisotropic with the grain shape factor $D_l/D_t \approx 9.8$. On the one hand, all the highly anisotropic bar-shaped grains lie in the plane, parallel to the texturing axis, i.e. some grain ordering takes place. On the other hand, the bars-grains lying in this plane are oriented randomly, i.e., the angle between the neighboring bars-grains changes randomly. Besides, each bar grain is rotated around its long axis by a random angle, too. As result, crystal a and b axes of the different bars-grains are oriented randomly. However, the crystal c-axis of irregular shape grains are preferentially oriented along the texturing axis. Ordering of these grains can be responsible for weak texturing in 1D sample. The colors of the grains in EBSD-SEM images taken from parallel surfaces of 1D and 2D samples are in agreement with texturing discussed above. Analysis of pole figures plotted from EBSD-
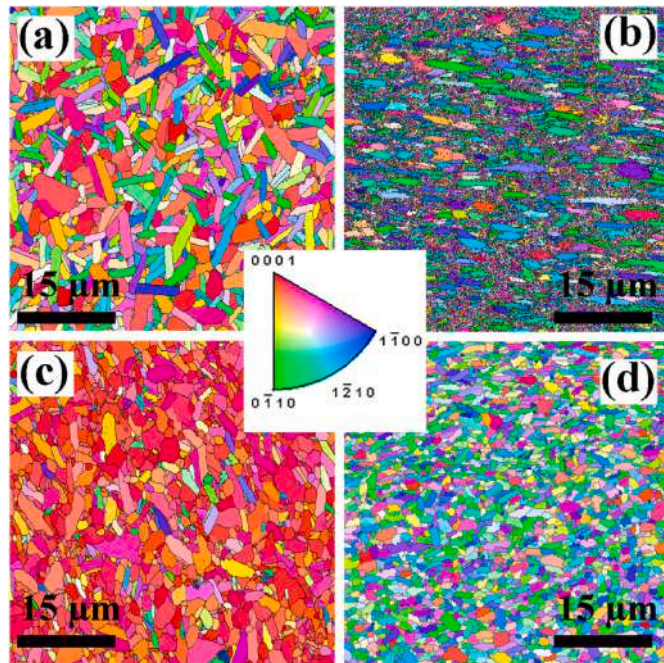
Fig. 7. EBSD-SEM maps, taken from the surfaces, oriented perpendicularly ((a) and (c)) parallel ((b) and (d)) to texturing axis for weakly-textured 1D ((a) and (b)) and highly-textured 2D ((c) and (d)) samples. The inset shows a link between the color of the drain and its crystallographic orientation. (For interpretation of the references to color in this figure legend, the reader is referred to the Web version of this article.)

SEM maps (Figs. S6 and S7) allowed estimating grain ordering degrees for samples. These estimates are by the values of the Lotgering factor (Table 1).

3.3. Feature in the thermoelectric properties of 1D and 2D samples

All the thermoelectric properties (ρ, S, and k_t) for 1D and 2D samples were measured for perpendicular and parallel measuring orientations. Under perpendicular or parallel measuring orientations, these properties were taken along directions, perpendicular or parallel to the SPS-pressing direction, respectively. As was mentioned above, for the highly-textured 2D $Bi_2Te_{2.7}Se_{0.3}$ sample, the SPS-pressing direction coincides with texturing axis. The transport ρ and k_t properties for textured Bi_2Te_3-based materials are known to be remarkably dependent on measuring orientation [45–50]. This orientation ρ and k_t dependence originated from anisotropy in these properties, which is inherent for Bi_2Te_3-based materials. Owing to specific features of chemical bonding in these materials, which include strong polar covalent and weak Van-der-Waals interactions, the crystal structure of materials is layered [51,52]. The layers are positioned perpendicularly to the crystal c-axis, hence, crystal (a–b)-planes are parallel to the layers. The transport ρ and k_t properties, taken along the layers and determined by the properties, which are characteristic for the (a–b)-planes (ρ_{ab} and k_{tab}), are remarkably different from the transport properties, taken perpendicularly to the layers and determined by the properties, which are characteristic for the c-axis (ρ_c and k_{tc}). Crystal anisotropy in the transport properties of Bi_2Te_3-based materials can be expressed as $\rho_c/\rho_{ab} \approx 5 \div 5.5$ and $k_{tab}/k_{tc} \approx 2$ [53–55]. In contrast to ρ and k_t, the Seebeck coefficient is a very weakly anisotropic property, i.e. $S_{ab} \approx S_c$. Naturally, anisotropy in ρ and k_t described will be inherent to single-crystalline Bi_2Te_3-based materials. In grained materials with disordered grain structures (all the grains are randomly oriented), the transport ρ and k_t properties will be already isotropic. Under texturing, grain ordering resulting in relevant preferential orientation of grains will occur. In turn, this grain order should be accompanied by a partial recovery in crystal anisotropy in the transport properties.

The $\rho(T)$ dependences for weakly-textured 1D and highly-textured 2D samples under perpendicular and parallel measuring orientations, are shown in Fig. 8 (a). For both measuring orientations, ρ steadily grows with increasing T. This $\rho(T)$ behavior is characteristic of degenerate semiconductors. The specific electrical resistance of the donor semiconductor is expressed as [56].

$$\rho = \frac{1}{e\mu_e n} \tag{2}$$

where e, n, and μ_e are the unit charge, concentration, and mobility of electrons, respectively.

For degenerate semiconductors, n is T-independent, and the $\rho(T)$ behavior is related to the $\mu_e(T)$ changes. Usually, the ρ growth with increasing T above room temperature is due to electron scattering on acoustic and optical phonons, resulting in decreasing μ_e. Anisotropy in the $\rho(T)$ behavior is observed for 1D and 2D samples. For both samples, the specific electrical resistivity within the whole temperature interval under study is higher for parallel measuring orientation as compared to that for perpendicular measuring orientation. The highest ρ (~13.5 μΩ m at room temperature) is observed for the 1D sample under parallel measuring orientation, whereas the lowest ρ (~6.5 μΩ m) corresponds to the 2D sample under perpendicular measuring orientation. Therefore, the specific electrical resistivity of samples being studied is remarkably dependent on (i) the dimension, size, and shape of the grains, and (ii) measuring orientation.

For highly-textured samples, the anisotropy in ρ observed was expected. Due to heavy texturing, the crystal c-axis of the grains in these samples are preferentially oriented along the SPS-pressing direction that is the texturing axis. Therefore, ρ_{II} measured for perpendicular
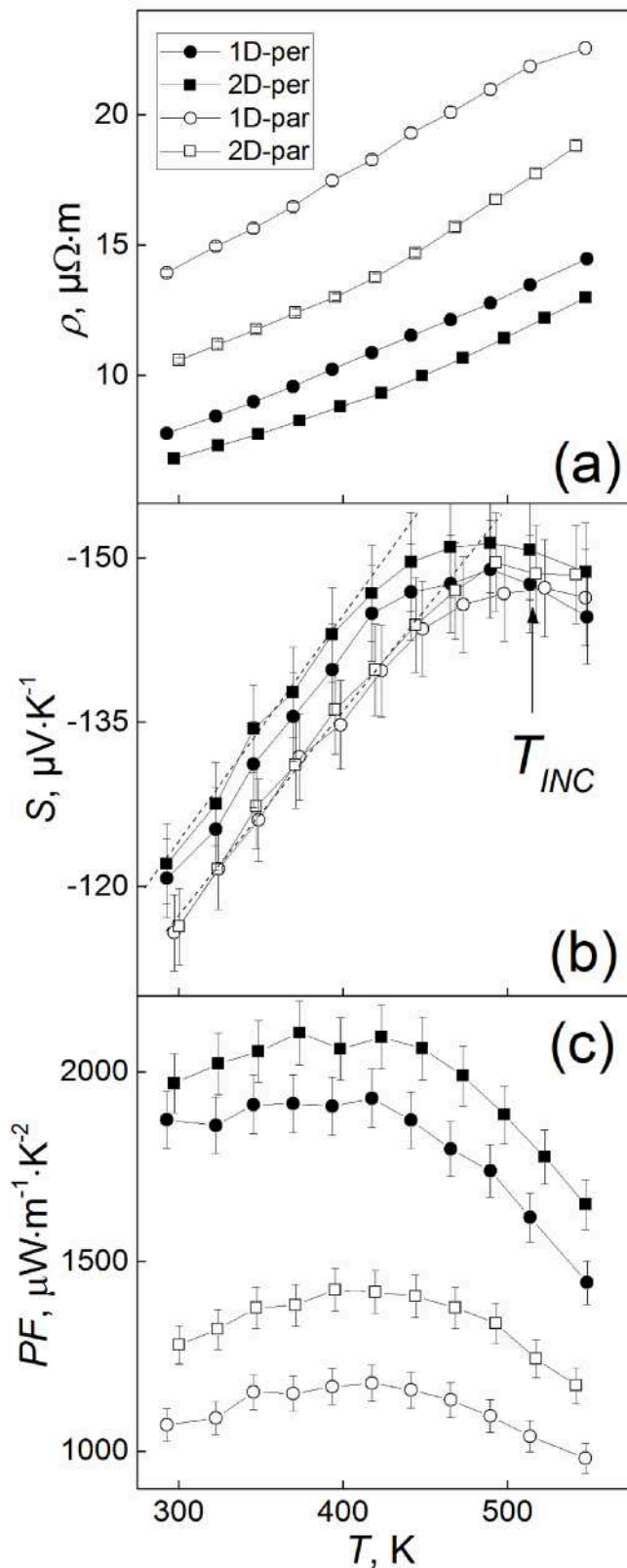
Fig. 8. Temperature dependences of the specific electrical resistivity (a), the Seebeck coefficient (b), and the power factor (c), taken for 1D and 2D $Bi_2Te_{2.7}Se_{0.3}$ samples under perpendicular and parallel measuring orientations.

measuring orientation will be dominantly contributed from the ρ_c resistivity. For parallel measuring orientation, ρ_{ab} will be already dominant contribution to $\rho_\perp$, since crystal (*a*–*b*)-planes of the grains lie preferentially in the plane, parallel to the SPS-pressuring direction. Taking into account the $\rho_c > \rho_{ab}$ ratio, which is specific for Bi_2Te_3-based materials, the experimental $\rho_\perp > \rho_{II}$ ratio, found for highly-textured 2D sample (Fig. 7 (a)), can be easily explained.

High anisotropy in ρ was surprisingly found in weakly-textured 1D $Bi_2Te_{2.7}Se_{0.3}$ sample, too. Generally, ρ in weakly-textured samples should be weakly dependent on measuring orientation. However, similarly to the highly-textured 2D sample, ρ in the weakly-textured 1D sample happened to be higher for parallel measuring orientation as compared to that for perpendicular measuring orientation. Moreover, anisotropy in ρ, expressed by a $\rho_{||}/\rho_\perp$ coefficient, was found to be even slightly higher for the weakly-textured sample (Table 1). Obviously, another mechanism, but partial recovering in crystal anisotropy, should be responsible for anisotropy in ρ, observed in weakly-textured 1D $Bi_2Te_{2.7}Se_{0.3}$ sample. Anisotropic grain size effect on the specific electrical resistivity can be considered as this mechanism [57].

Grain boundaries in a grained material are known to be effective scattering centers for electrons and phonons, which strongly affect the specific electrical resistivity and thermal conductivity, respectively. Grain-boundary scattering effect on the transport ρ and k_t properties is crucially dependent on grain size. Usually, this effect is characteristic of nano- and micro-grained materials and it remarkably enhances with decreasing in the grain size. Grain boundary scattering of electrons results in reducing in electron mobility. A link between the electron mobility, μ_{gb}, which is due to grain boundary scattering, and the grain size, D, is expressed as [58].

$$\mu_{gb} = \frac{D/l_e}{1 + D/l_e}\mu_0 \qquad (3)$$

where l_e is the electron mean free path and μ_0 is the electron mobility, characteristic of a grainless material.

By expression (3), decreasing in D will result in a relevant decrease in μ_{gb}. If the grain sizes in different directions are different, too, the grain size effect on ρ and k_t can be an anisotropic one because it will be dependent on the measuring ρ and k_t orientations. This anisotropy in ρ and k_t is due to different numbers of the grain boundaries, overcome by the electrons or phonons under different measuring orientations. Less grain size will correspond to higher ρ and lower k_t for relevant measuring orientation. Anisotropic grain size effect on ρ, observed in textured $Bi_{1.9}Gd_{0.1}Te_3$ material, was recently analyzed in Ref. [57] For the $Bi_2Te_{2.7}Se_{0.3}$ material, the difference in the grain size for the perpendicular and parallel measuring orientations takes place for weakly-textured 1D and highly-textured 2D samples. This difference can be characterized by a grain shape factor, D_l/D_t (Table 1). The D_l and D_t sizes correspond to the perpendicular and parallel measuring orientations, respectively. Since $D_l > D_t$, the $\rho_{||}$ resistivity should be higher than the $\rho_\perp$ resistivity. Thus, besides anisotropy in ρ, which is due to recovering in crystal anisotropy via texturing (this mechanism should be dominant in highly-textured 2D sample), additional anisotropy in ρ seems to be originated from the anisotropic grain size effect on ρ. This anisotropic grain size effect on ρ can be responsible for anisotropy in ρ, observed in the weakly-textured 1D sample. It should be also mentioned that the 1D sample is Te-rich, whereas the 2D sample is Te-deficient. As was mentioned above, the nature of point defects in Te-rich and Te-deficient samples are different. Interstitial Te atoms and anti-site Te_{Bi} defects are specific for the Te-rich composition, and Te-vacancies and anti-site Bi_{Te} defects are specific for the Te-deficient composition. Moreover, as was shown earlier [59], the electron mobility in the Te-rich $Bi_{2-x}Gd_xTe_3$ compound is remarkably lower as compared to that for the Te-deficient compound. Therefore, one can conclude that interstitial Te atoms and anti-site Te_{Bi} defects are more effective scattering centers for electrons than Te-vacancies and anti-site Bi_{Te} defects. Then, the electron

mobility in 1D and 2D samples will be different and the specific electrical resistivity of the 1D sample should be higher than ρ of the 2D sample. Texturing effect on ρ and anisotropic grain size effect on ρ just result in the development of anisotropy in the specific electrical resistivity.

The $S(T)$ curves, taken for 1D and 2D samples under perpendicular and parallel measuring orientations are positioned very close to each other (Fig. 8 (b)). Since the majority of carriers in the samples being studied are electrons, the Seebeck coefficient is negative. All the $S(T)$ dependences in Fig. 8 (b) are bell-shaped. Tops of the bells are located at temperature $T_{INC} \approx 500$ K. The Seebeck coefficient of degenerate semiconductor is expressed as [60].

$$S = \frac{2k_B^2 T m^*}{3eh^2}\left(\frac{\pi}{3n}\right)^{2/3}\left(\frac{3}{2}+\gamma\right) \tag{4}$$

where k_B is the Boltzmann's constant, $\hbar$ is the reduced Planck constant, m^* is the density-of-state effective mass of electrons and γ is the scattering factor.

As shown by dashed lines, all the $S(T)$ dependences are T-linear below T_{INC}, which is in agreement with expression (4). But above T_{INC}, bipolar effect contribution to the $S(T)$ behavior becomes the dominant one. At the bipolar effect, electrons and holes are simultaneously presented in semiconductors. Thermal excitation of electron-hole pairs due to intrinsic conductivity does not change the majority carriers' concentration too much. However, minority carriers' concentration will be remarkably increasing. The S sign for the holes is positive. Competing of two contributions into S with opposite signs results in forming of the $S(T)$ maxima. The temperature dependences of the power factor, $PF = S^2/\rho$, are shown in Fig. 8 (c). Since the $S(T)$ dependences for 1D and 2D samples and all measuring orientations are very close, the $PF(T)$ behavior is governed by the $\rho(T)$ behavior. The PF is highest for the 2D sample and at perpendicular measuring orientation (in this case ρ is lowest). The PF is lowest for the 1D sample and at parallel measuring orientation (in this case ρ is highest).

The $k_t(T)$ dependences, taken for 1D and 2D samples under perpendicular and parallel measuring orientations, are shown in Fig. 9 (a). For both type's samples, the thermal conductivity is higher for perpendicular measuring orientation as compared to that for parallel measuring orientation. Anisotropy in k_t, expressed by a $k_{t\perp}/k_{t||}$ coefficient, was found to be the same for 1D and 2D samples (Table 1). For a weakly-textured 1D sample, this anisotropy in k_t can be related to the anisotropic grain size effect on k_t, whereas for a highly-textured 2D sample the anisotropy in k_t is developing via texturing. All the $k_t(T)$ curves demonstrating minimum at T_{INC} are typical for Bi_2Te_3-based compounds [61–64]. In general, the total thermal conductivity includes the phonon thermal conductivity, k_p, the electronic thermal conductivity, k_e, and the bipolar thermal conductivity, k_b. It is known that k_e contribution is related to the specific electrical conductivity, $\sigma = 1/\rho$, by the Wiedemann-Franz law [65].

$$k_e = L\sigma T \tag{5}$$

where L is the Lorenz number.

According to the approach, proposed in Ref. [66], L and maximum S value, $|S|_{max}$, are linked as

$$L\left[10^{-8}, W \bullet \Omega \bullet K^{-2}\right] = 1.5 + \exp\left(-\frac{|S|_{max}\left[\mu V \bullet K^{-1}\right]}{116}\right) \tag{6}$$

By using expression (6), L was estimated as $\sim 1.8 \times 10^{-8}$ $W\Omega \cdot K^{-2}$ for 1D and 2D samples. Using this L value, the $k_e(T)$ contributions into k_t for 1D and 2D samples under perpendicular and parallel measuring orientations were extracted (Fig. 8 (b)). These $k_e(T)$ contributions are correlated with the $\rho(T)$ dependences, presented in Fig. 7 (a), i.e., k_e for the 2D sample, taken for perpendicular measuring orientation, is highest, whereas k_e for the 1D sample, taken for parallel measuring orientation, is lowest.
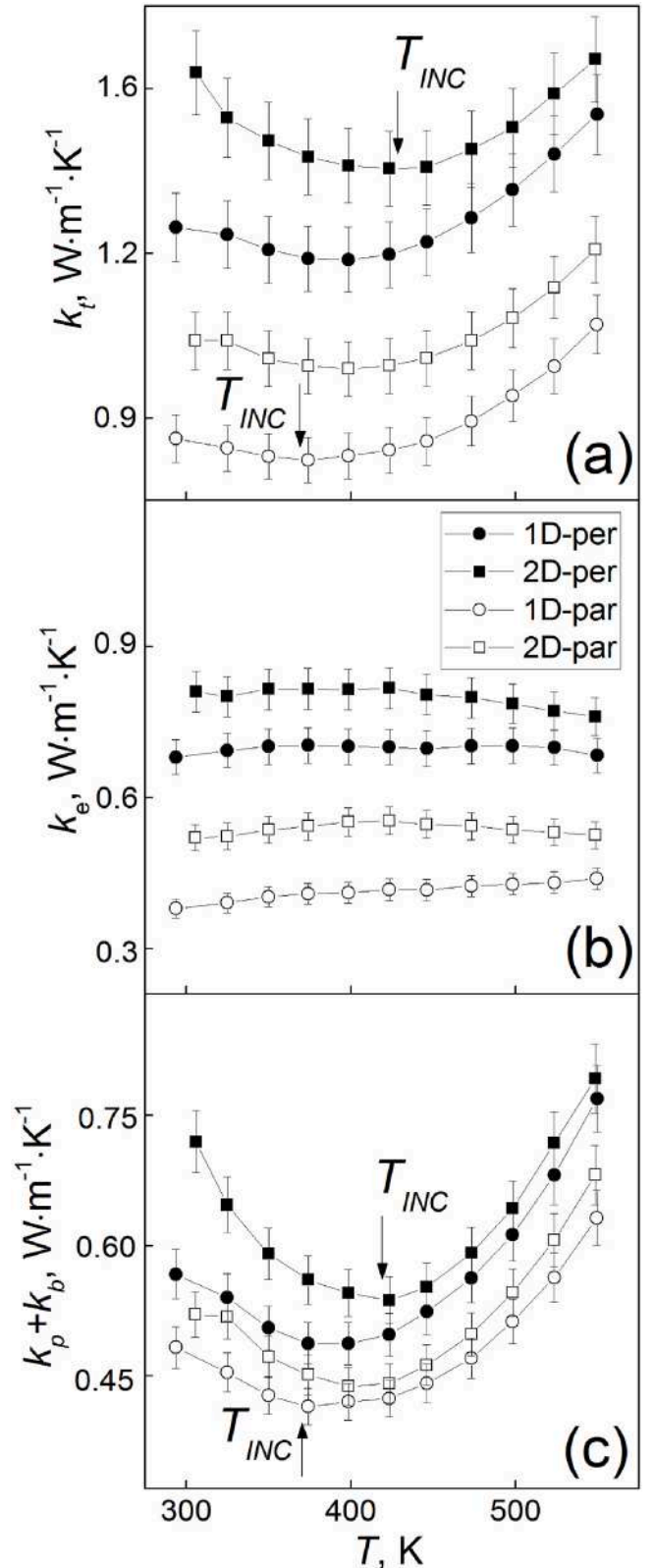
Fig. 9. Temperature dependences of the total thermal conductivity (a), the contribution from the electronic thermal conductivity (b), and the summarized contributions from the phonon and bipolar thermal conductivity (c), taken for 1D and 2D $Bi_2Te_{2.7}Se_{0.3}$ samples under perpendicular and parallel measuring orientations.

Then, sums of the lattice and bipolar thermal conductivity contributions, $k_p(T)+k_b(T) = k_t(T)-k_e(T)$, were found (Fig. 9 (c)). Similarly to the $k_t(T)$ dependences, these summarized contributions have minima at T_{INC}, too. Below T_{INC}, the thermal conductivity is due to the lattice thermal conductivity. It is known that above the Debye temperature the lattice thermal conductivity decreases with increasing T obeying a T^{-1} law [56]. By the Dulong-Petit law, the phonon-specific heat is T-independent. With increasing T, phonon energy and the number of phonons linearly increase. The phonon scattering rate is proportional to this number. As result, k_p also decreases with increasing T. This mechanism is responsible for the $k_p(T)+k_b(T)$ behavior, observed below T_{INC}. The lattice thermal conductivity happened to be very low (~0.4 at ~375 K) for the 1D sample and at parallel measuring orientation.

Above T_{INC}, the summarized $k_p(T)+k_b(T)$ contributions already increase with increasing T. This behavior originated from bipolar thermal conductivity. In this case, electron-hole pairs are thermally excited at the hot side of the semiconductor sample. Next, these pairs move to the cold side, where they are recombined. The energy of recombination per one pair will be equal to or greater than the band gap. This energy corresponds to a phonon, transferring heat. The bipolar thermal conductivity is expressed as [67].

$$k_b = \frac{\sigma_n \bullet \sigma_p}{\sigma_n + \sigma_p}(S_p - S_n)^2 T \qquad (7)$$

where σ_i and S_i (subscript $i = n, p$) are the partial electrical conductivity and Seebeck coefficient for electrons and holes, respectively. In turn, σ_i of each carrier is $\sigma_i = ie\mu_i$ where $i=n, p$ designates the electron and hole concentration, respectively.

It should be noted that the values of T_{INC} in the $S(T)$ (Fig. 8 (b)) and $k_t(T)$ (Fig. 9 (a)) dependences are different, although both the $S(T)$ maxima and the $k_t(T)$ minima are related to the bipolar effects via intrinsic conductivity. Actually, T_{INC} does not correspond to the correct temperature of the onset of intrinsic thermal conductivity. Moreover, T_{INC} is also dependent on the type of sample (1D sample or 2D sample) and measuring orientation (perpendicular or parallel orientations). These features in the $k_t(T)$ dependences are connected to relevant features in the $k_p(T)+k_b(T)$ behavior (Fig. 9 (c)). In particular, the k_b contribution is related to σ_i and S_i, which, in turn, are dependent on the type of sample and measuring orientation. By now, these dependencies were not studied in detail.

The ρ, S, and k_t values were applied to plot the $ZT(T)$ dependencies (Fig. 10). All the dependencies are bell-shaped. Forming of the $ZT(T)$ maxima at T_{INC} is also related to high-temperature intrinsic thermal conductivity. The highest $ZT \approx 0.68$ (at ~450 K) was observed for 1D and 2D samples and at perpendicular measuring orientation. In this case, the $ZT(T)$ curves are positioned very close to each other. The $ZT(T)$ curves, taken for 1D and 2D samples at parallel measuring orientation, are positioned a bit below. These features in the $ZT(T)$ behavior directly originated from the temperature ρ, S, and k_t behavior, presented in Figs. 8 and 9.

4. Conclusion

Thus, weakly-textured Te-rich 1D and highly-textured Te-deficient 2D samples of thermoelectric $Bi_2Te_{2.7}Se_{0.3}$ compound were prepared by using spark plasma sintering of staring powders with different morphology of the particles. The 1D sample consisted of bar-shaped grains, and the bars were elongated along the crystal c-axis. The 2D sample preferentially consisted of plate-shaped grains, and the plates were oriented perpendicularly to the crystal c-axis. Both the bar-shaped grains and the plate-shaped grains are located in lamellar sheets, which are perpendicular to the SPS-pressing direction. Although the shape of the bars-grains is highly anisotropic, they are oriented randomly within the lamellar sheets. Besides the bars-grains, grains having irregular shapes are also forming in the 1D sample. Ordering of these grains
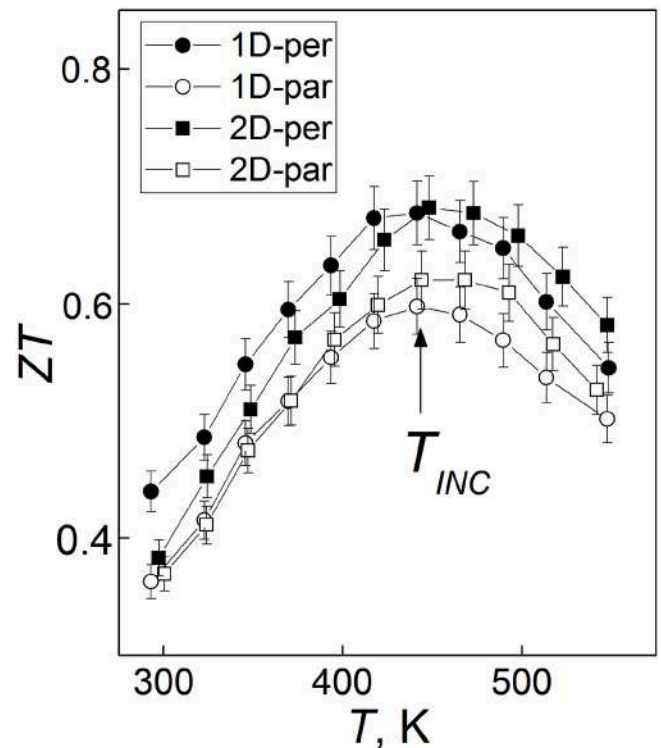
Fig. 10. Temperature dependences of the thermoelectric figure-of-merit, taken for 1D and 2D $Bi_2Te_{2.7}Se_{0.3}$ samples under perpendicular and parallel measuring orientations.

results in weak texturing, observed in the 1D sample. Due to texturing, crystal c-axes of the grains are preferentially oriented along the SPS-pressing direction, which coincides with texturing axis. Both the 1D sample and 2D sample show anisotropy in the behavior of the specific electrical conductivity and the total thermal conductivity. For weakly-textured 1D sample, this unexpected anisotropy can be originated from the anisotropic grain size effect on the transport properties. The highest value of the thermoelectric figure-of-merit (~0.68) was found for 1D and 2D samples and at perpendicular measuring orientation. The main high-temperature features in the behavior of the Seebeck coefficient and the total thermal conductivity are related to bipolar effects.

Credit author statement

Maxim Yaprintsev: Project administration, Investigation, Alexei Vasil'v: Investigation, Oleg Ivanov: Conceptualization, Writing - review & editing, Daniil Popkov: Investigation, Egor Kudryavtsev: Investigation.

Declaration of competing interest

The authors declare that they have no known competing financial interests or personal relationships that could have appeared to influence the work reported in this paper.

Data availability

Data will be made available on request.

Acknowledgments

University « Technology and Materials» with financial support from the Ministry of Science and Higher Education of the Russian Federation within the framework of agreement No. 075-15-2021-690 (unique identifier for the project RF——2296.61321X0030).

Appendix A. Supplementary data

Supplementary data to this article can be found online at https://doi.org/10.1016/j.solidstatesciences.2022.107083.

References

[1] D. Wolf, J. Lutsko, M. Kluge, Physical properties of grain-boundary materials: comparison of EAM and central-force potentials, in: V. Vitek, D.J. Srolovitz (Eds.), Atomistic Simulation of Materials, Springer, Boston, 1989, pp. 245–263.

[2] T. Watanabe, Grain boundary engineering: historical perspective and future prospects, J. Mater. Sci. 46 (2011) 4095–4115.

[3] I.P. Semenova, R.Z. Valiev, E.B. Yakushina, G.H. Salimgareeva, T.C. Lowe, Strength and fatigue properties enhancement in ultrafine-grained Ti produced by severe plastic deformation, J. Mater. Sci. 4 (2008) 7354–7359, https://doi.org/10.1007/s10853-008-2984-4.

[4] N. Vandewalle, G. Lumay, O. Gerasimov, F. Ludewig, Influence of grain shape, friction and cohesion on granular compaction dynamics, Eur. Phys. J. E. 22 (2007) 241–248, https://doi.org/10.1140/epje/e2007-00031-0.

[5] H.K. Lee, H. Baier, J.S. Park, Y.P. Lee, Y.S. Lee, Grain-size effects and the physical properties of $La_{0.7}Ca_{0.3}MnO_{3-\delta}$, Key Eng. Mater. 277–279 (2005) 929–934, https://doi.org/10.4028/www.scientific.net/kem.277-279.929.

[6] M. Becton, X. Wang, Grain-size dependence of mechanical properties in polycrystalline boron-nitride: a computational study, Phys. Chem. Chem. Phys. 17 (2015) 21894–21901, https://doi.org/10.1039/C5CP03460D.

[7] A. Isacsson, A.W. Cummings, L. Colombo, L. Colombo, J.M. Kinaret, S. Roche, Scaling properties of polycrystalline graphene: a review, 2D Mater. 4 (2017) 1–12, https://doi.org/10.1088/2053-1583/aa5147, 012002.

[8] M.A. Meyers, A. Mishra, D.J. Benson, Mechanical properties of nanocrystalline materials, Prog. Mater. Sci. 51 (2006) 427–556, https://doi.org/10.1016/j.pmatsci.2005.08.003.

[9] D. Choi, The electron scattering at grain boundaries in tungsten films, Microelectron. Eng. 122 (2014) 5–8, https://doi.org/10.1016/j.mee.2014.03.012.

[10] H. Zeng, Y. Wu, J. Zhang, C. Kuang, M. Yue, S. Zhou, Grain size-dependent electrical resistivity of bulk nanocrystalline Gd metals, Prog. Nat. Sci. Mater. Int. 23 (2013) 18–22, https://doi.org/10.1016/J.PNSC.2013.01.003.

[11] A.J. Minnich, M.S. Dresselhaus, Z.F. Ren, G. Chen, Bulk nanostructured thermoelectric materials: current research and future prospects, Energy Environ. Sci. 2 (2009) 466–479, https://doi.org/10.1039/b822664b.

[12] M.G. Kanatzidis, Nanostructured thermoelectrics: the new paradigm, Chem. Mater. 22 (2009) 648–659, https://doi.org/10.1021/cm902195j.

[13] Z.G. Chen, G. Han, L. Yang, L. Cheng, J. Zou, Nanostructured thermoelectric materials: current research and future challenge, Prog. Nat. Sci. Mater. Int. 22 (2012) 535–549, https://doi.org/10.1016/j.pnsc.2012.11.011.

[14] C.J. Vineis, A. Shakouri, A. Majumdar, M.G. Kanatzidis, Nanostructured thermoelectrics: big efficiency gains from small features, Adv. Mater. 22 (2010) 3970–3980, https://doi.org/10.1002/adma.201000839.

[15] K. Kishimoto, Y. Nagamoto, T. Miki, T. Koyanagi, Microstructure and thermoelectric properties of Cr-doped β-FeSi$_2$ sintered with micrograins treated in radio frequency plasmas of SiH$_4$ and GeH$_4$ gases, J. Appl. Phys. 92 (2002) 4393–4401, https://doi.org/10.1063/1.1507814.

[16] C.H. Kuo, H.S. Chien, C.S. Hwang, Y.W. Chou, M.S. Jeng, M. Yoshimura, Thermoelectric properties of fine-grained PbTe bulk materials fabricated by cryomilling and spark plasma sintering, Mater. Trans. 52 (2011) 795–801, https://doi.org/10.2320/matertrans.M2010331.

[17] S.V. Novikov, A.T. Burkov, X. Tang, Y. Yan, Thermoelectric properties of melt-spun and crystalline $In_{0.2}Ce_{0.1}Co_4Sb_{12.3}$ ribbons, Mater. Today Proc. 8 (2019) 713–717.

[18] O. Ivanov, O. Maradudina, R. Lyubushkin, Grain size effect on electrical resistivity of bulk nanograined Bi$_2$Te$_3$ material, Mater. Char. 99 (2015) 175–179, https://doi.org/10.1016/j.matchar.2014.12.001 1044-5803.

[19] H. Wu, J. Carrete, Z. Zhang, Y. Qu, X. Shen, Z. Wang, L.D. Zhao, J. He, Strong enhancement of phonon scattering through nanoscale grains in lead sulfide thermoelectrics, NPG Asia Mater. 6 (2014) 2–11, https://doi.org/10.1038/am.2014.39, 2014.

[20] W. Kim, Strategies for engineering phonon transport in thermoelectrics, J. Mater. Chem. C 3 (2015) 336, https://doi.org/10.1039/C5TC01670C, 10348.

[21] Q.G. Zhang, X. Zhang, B.Y. Cao, M. Fujii, K. Takahashi, T. Ikuta, Influence of grain boundary scattering on the electrical properties of platinum nanofilms, Appl. Phys. Lett. 89 (2006) 1–3, https://doi.org/10.1063/1.2338885, 114102.

[22] M. Wei, X.-L. Shi, Z.-H. Zheng, F. Li, W.-D. Liu, L.-P. Xiang, Y.-S. Xie, Y.-X. Chen, J.-Y. Duan, H.-L. Ma, G.-X. Liang, X.-H. Zhang, P. Fan, Z.-G. Che, Directional thermal diffusion realizing inorganic Sb$_2$Te$_3$/Te hybrid thin films with high thermoelectric performance and flexibility, Adv. Funct. Mater. (2022) 1–9, 2207903.

[23] J.H. Bahk, Z. Bian, A. Shakouri, Electron energy filtering by a nonplanar potential to enhance the thermoelectric power factor in bulk materials, Phys. Rev. B 87 (2013) 1–13, https://doi.org/10.1103/PhysRevB.87.075204, 075204.

[24] R. Fortulan, S.A. Yamini, Recent progress in multiphase thermoelectric materials, Materials 14 (2021) 1–28, https://doi.org/10.3390/ma14206059.

[25] A.M. Dehkordi, M. Zebarjadi, J. He, T.M. Tritt, Thermoelectric power factor: enhancement mechanisms and strategies for higher performance thermoelectric materials, Mater. Sci. Eng. R Rep. 97 (2015) 1–22, https://doi.org/10.1016/j.mser.2015.08.001.

[26] S.D. Bhame, D. Pravarthana, W. Prellier, J.G. Noudem, Enhanced thermoelectric performance in spark plasma textured bulk n-type $Bi_2Te_{2.7}Se_{0.3}$ and p-type $Bi_{0.5}Sb_{1.5}Te_3$, Appl. Phys. Lett. 102 (2013) 1–3, https://doi.org/10.1063/1.4807771, 2190.

[27] Y. Li, F. Li, J. Dong, Z.H. Ge, F. Kang, J. He, H. Du, B. Li, J. Li, Enhanced mid-temperature thermoelectric performance of textured SnSe polycrystals made of solvothermally synthesized powders, J. Mater. Chem. C 4 (2016) 2047–2055, https://doi.org/10.1039/C5TC04202J.

[28] A. Novitskii, G. Guelou, D. Moskovskikh, A. Voronin, E. Zakharova, L. Shvanskaya, A. Bogach, A. Vasilev, V. Khovaylo, T. Mori, Reactive spark plasma sintering and thermoelectric properties of Nd-substituted BiCuSeO oxyselenides, J. Alloys Compd. 785 (2019) 96–104, https://doi.org/10.1016/j.jallcom.2019.01.183.

[29] A. Vasil'ev, M. Yaprintsev, O. Ivanov, E. Danshina, Anisotropic thermoelectric properties of $Bi_{1.9}Lu_{0.1}Te_{2.7}Se_{0.3}$ textured via spark plasma sintering, Solid State Sci. 84 (2018) 28–43, https://doi.org/10.1016/j.solidstatesciences.2018.08.004.

[30] Y. Liu, Y. Zhang, K.H. Lim, M. Ibáñez, S. Ortega, M. Li, J. David, S. Martí-Sánchez, K.M. Ng, J. Arbiol, M.V. Kovalenko, D. Cadavid, A. Cabot, High thermoelectric performance in crystallographically textured n-type $Bi_2Te_{3-x}Se_x$ produced from asymmetric colloidal nanocrystals, ACS Nano 12 (2018) 7174–7184, https://doi.org/10.1021/acsnano.8b03099.

[31] D.B. Kumar, B. Selva babu, K.M. Aravind Jerrin, N. Joseph, A. Jiss, Review of spark plasma sintering process, IOP Conf. Ser. Mater. Sci. Eng. 993 (2020) 1–8, https://doi.org/10.1088/1757-899X/993/1/012004, 012004.

[32] E.A. Olevskya, Consolidation enhancement in spark-plasma sintering: impact of high heating rates, J. Appl. Phys. 102 (2007) 1–5, https://doi.org/10.1063/1.2822189, 114913.

[33] M. Takashiri, K. Miyazaki, S. Tanaka, J. Kurosaki, D. Nagai, H. Tsukamoto, Effect of grain size on thermoelectric properties of n-type nanocrystalline bismuth-telluride based thin films, J. Appl. Phys. 104 (2008) 1–6, https://doi.org/10.1063/1.2990774, 084302.

[34] H.J. Goldsmid, Bismuth telluride and its alloys as materials for thermoelectric generation, Mater 7 (2014) 2577–2592, https://doi.org/10.3390/ma7042577.

[35] S. Li, Z. Huang, R. Wang, C. Wang, W. Zhao, N. Yang, F. Liu, J. Luo, Y. Xiao, F. Pan, Precision grain boundary engineering in commercial $Bi_2Te_{2.7}Se_{0.3}$ thermoelectric materials towards high performance, J. Mater. Chem. A. 9 (2021) 11442–11449, https://doi.org/10.1039/D1TA01016F.

[36] T. Liu, W. Zhu, R. Wang, S. Li, Y. Xiao, Improvement of thermoelectric performance of $Bi_2Te_{2.7}Se_{0.3}$ via grain boundary engineering with melting, KOH 12 (2019), https://doi.org/10.1142/S1793604719500826.

[37] M.M. Alsalama, H. Hamoudi, A. Abdala, Z.K. Ghouri, K.M. Youssef, Enhancement of thermoelectric properties of layered chalcogenide materials, Rev. Adv. Mater. Sci. 59 (2020) 371–398, https://doi.org/10.1515/rams-2020-0023.

[38] F.J. Humphreys, M. Hatherly, Recrystallization and Related Annealing Phenomena, Elsevier, Oxford, UK, 2004.

[39] J. Lee, A. Berger, L.U. Cagnon, U. Gosele, K. Nielsch, J. Lee, Disproportionation of thermoelectric bismuth telluride nanowires as a result of the annealing process, Phys. Chem. Chem. Phys. 12 (2010) 15247–15250, https://doi.org/10.1039/c0cp00749h.

[40] P. Lost'ák, C. Drasar, D. Bachan, L. Benes, A. Krejcová, Defects in $Bi_2Te_{3-x}Se_x$ single crystals, Radiat. Eff. Defect Solid 165 (2010) 211–215, https://doi.org/10.1080/10420151003616663.

[41] T. Zhu, L. Hu, X. Zhao, J. He, New insights into intrinsic point defects in V$_2$VI$_3$ thermoelectric materials, Adv. Sci. 3 (2016) 1–16, https://doi.org/10.1002/advs.201600004, 1600004.

[42] S.-W. Kim, M.-H. Jung, Gd doping effect in p-type Bi$_2$Te$_3$ single crystals, AIP Adv. 8 (2018), 101319, https://doi.org/10.1063/1.5042494-1-6.

[43] F.K. Lotgering, Topotactical reactions with ferrimagnetic oxides having hexagonal crystal structures—I, J. Inorg. Nucl. Chem. 9 (1959) 113–123, https://doi.org/10.1016/0022-1902(59)80070-1.

[44] R.D. Shannon, Revised effective ionic radii and systematic studies of interatomic distances in halides and chaleogenides, Acta Crystallogr. A32 (1976) 751–767, https://doi.org/10.1107/S0567739476001551.

[45] O. Ivanov, M. Yaprintsev, A. Vasil'ev, Comparative analysis of the thermoelectric properties of the non-textured and textured $Bi_{1.9}Gd_{0.1}Te_3$ compounds, J. Solid State Chem. 290 (2020) 1–10, https://doi.org/10.1016/j.jssc.2020.121559, 121559.

[46] X.A. Fan, J.Y. Yang, R.G. Chen, H.S. Yun, W. Zhu, S.Q. Bao, X.K. Duan, Characterization and thermoelectric properties of p-type 25%Bi$_2$Te$_3$–75%Sb$_2$Te$_3$ prepared via mechanical alloying and plasma activated sintering, J. Phys. D Appl. Phys. 39 (2006) 740–745, https://doi.org/10.1088/0022-3727/39/4/021.

[47] J. Jiang, L. Chen, S. Bai, Q. Yao, Q. Wang, Fabrication and thermoelectric performance of textured n-type Bi$_2$(Te,Se)$_3$ by spark plasma sintering, Mater. Sci. Eng. B 117 (2005) 334–338, https://doi.org/10.1016/j.mseb.2005.01.002.

[48] Q. Lognon, F. Gascoin, O.I. Lebedev, L. Lutterotti, S. Gascoin, D. Chateigner, Quantitative texture analysis of spark plasma textured n-Bi$_2$Te$_3$, J. Am. Ceram. Soc. 97 (2014) 2038–2045, https://doi.org/10.1111/jace.12970/.

[49] M. Yaprintsev, A. Vasil'ev, O. Ivanov, Thermoelectric properties of the textured $Bi_{1.9}Gd_{0.1}Te_3$ compounds spark-plasma-sintered at various temperatures, J. Eur. Ceram. Soc. 40 (2020) 742–750, https://doi.org/10.1016/j.jeurceramsoc.2018.12.041.

[50] O. Ivanov, M. Yaprintsev, A. Vasil'ev, E. Yaprintseva, Microstructure and thermoelectric properties of the medium-entropy block-textured $BiSbTe_{1.5}Se_{1.5}$ alloy, J. Alloys Compd. 872 (2021) 1–7, https://doi.org/10.1016/j.jallcom.2021.159743, 159743.

[51] J.R. Drabble, C.H.L. Goodman, Chemical bonding in bismuth telluride, J. Phys. Chem. Solid. 5 (1958) 142–144, https://doi.org/10.1016/0022-3697(58)90139-2.

[52] S. Nakajima, The crystal structure of $Bi_2Te_{3-x}Se_x$, J. Phys. Chem. Solid. 24 (1963) 479–485, https://doi.org/10.1016/0022-3697(63)90207-5.

[53] O. Ben-Yehuda, R. Shuker, Y. Gelbstein, Z. Dashevsky, M.P. Dariel, Highly textured Bi_2Te_3-based materials for thermoelectric energy conversion, J. Appl. Phys. 101 (2007) 1–6, https://doi.org/10.1063/1.2743816, 113707.

[54] J.J. Shen, L.P. Hu, T.J. Zhu, X.B. Zhao, The texture related anisotropy of thermoelectric properties in bismuth telluride based polycrystalline alloys, Appl. Phys. Lett. 99 (2011) 1–3, 124102, https://doi: 10.1063/1.3643051.

[55] G.S. Nolas, J. Sharp, H.J. Goldsmid, Thermoelectrics Basic Principles and New Materials Developments, Springer, Berlin, 2001.

[56] J.S. Blakemore, Solid State Physics, Cambridge University Press, Cambridge, 1985.

[57] O. Ivanov, M. Yaprintsev, A. Vasil, ev, Anisotropy of the grain size effect on the electrical resistivity of n-type $Bi_{1.9}Gd_{0.1}Te_3$ thermoelectric textured by spark plasma sintering, J. Eur. Ceram. Soc. 40 (2020) 3431–3436, https://doi.org/10.1016/j.jeurceramsoc.2020.03.048.

[58] L.P. Bulat, I.A. Drabkin, V.V. Karataev, V.B. Osvenskii, D.A. Pshenai-Severin, Effect of boundary scattering on the thermal conductivity of a nanostructured semiconductor material based on the $Bi_xSb_{2-x}Te_3$ solid solution, Phys. Solid State 52 (2010) 1836–1841.

[59] M. Yaprintsev, A. Vasil'ev, O. Ivanov, Preparation and characterization of nonstoichiometric Te-deficient and Te-rich thermoelectric $Bi_{2-x}Gd_xTe_{3\pm y}$

[60] K.C. Lukas, W.C. Liu, Z.F. Ren, C.P. Opeil, Transport properties of Ni, Co, Fe, Mn doped $Cu_{0.01}Bi_2Te_{2.7}Se_{0.3}$ for thermoelectric device applications, J. Appl. Phys. 112 (2012) 1–5, https://doi.org/10.1063/1.4749806, 054509.

[61] M. Yapryntsev, A. Vasil'ev, O. Ivanov, Sintering temperature effect on thermoelectric properties and microstructure of the grained $Bi_{1.9}Gd_{0.1}Te_3$ compound, J. Eur. Ceram. Soc. 39 (2019) 1193–1205, https://doi.org/10.1016/j.jeurceramsoc.2018.12.041.

[62] J. Yang, F. Wu, Z. Zhu, L. Yao, H. Song, X. Hu, Thermoelectrical properties of lutetium-doped Bi_2Te_3 bulk samples prepared from flower-like nanopowders, J. Alloys Compd. 619 (2015) 401–405, https://doi.org/10.1016/j.jallcom.2014.09.024.

[63] X.H. Ji, X.B. Zhao, Y.H. Zhang, B.H. Lu, H. Ni, Synthesis and properties of rare earth containing Bi_2Te_3 based thermoelectric alloys, J. Alloys Compd. 387 (2005) 282–286, https://doi.org/10.1016/j.jallcom.2004.06.047.

[64] F. Wu, H. Song, J. Jia, X. Hu, Effects of Ce, Y, and Sm doping on the thermoelectric properties of Bi_2Te_3 alloy, Prog. Nat. Sci. Mater. Int. 23 (2013) 408–412, https://doi.org/10.1016/j.pnsc.2013.06.007.

[65] W. Liu, X. Yan, G. Chen, Z. Ren, Recent advances in thermoelectric nanocomposites, Nano Energy 1 (2012) 42–56, https://doi.org/10.1021/acs.jpcc.0c01311.

[66] H. Kim, Z. Gibbs, Y. Tang, H. Wang, G. Snyder, Characterization of Lorenz number with Seebeck coefficient measurement, Apl. Mater. 3 (2015) 1–5, https://doi.org/10.1063/1.4908244, 041506.

[67] S. Wang, J. Yang, T. Toll, J. Yang, W. Zhang, X. Tang, Conductivity-limiting bipolar thermal conductivity in semiconductors, Sci. Rep. 5 (2015) 1–5, https://doi.org/10.1038/srep10136, 10136.